

Graphite Felt-Sandwiched Ni/SiC Catalysts for the Induction Versus Joule-Heated Sabatier Reaction: Assessing the Catalyst Temperature at the Nanoscale

Lai Truong-Phuoc,* Cuong Duong-Viet, Giulia Tuci, Andrea Rossin, Jean-Mario Nhut, Walid Baaziz, Ovidiu Ersen, Mehdi Arab, Alex Jourdan, Giuliano Giambastiani,* and Cuong Pham-Huu*



Cite This: <https://doi.org/10.1021/acssuschemeng.1c07217>



Read Online

ACCESS |



Metrics & More



Article Recommendations

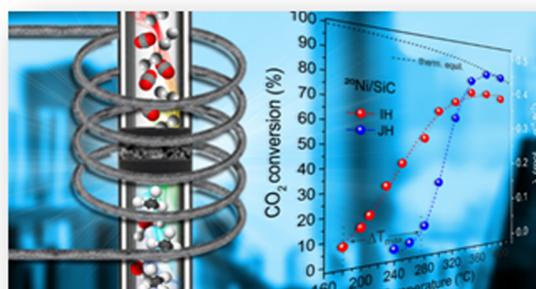


Supporting Information

ABSTRACT: The paper describes a series of graphite felt-sandwiched ^kNi/SiC composites at variable metal loading ($k = 10$, 15, and 20 wt %) and their application as catalysts for the CO₂ methanation process (Sabatier reaction) under two distinct and conceptually different heating setups: Joule heating versus induction heating (IH). A comparative analysis carried out on all catalysts from this series operated under the two heating configurations has unveiled the superior performance of radiofrequency (RF)-heated (IH) catalysts in the process. Most importantly, it has offered a practical tool to map the gap existing between the macroscopic temperature value measured at the catalyst bed using a remote-sensing thermometer (pyrometer) and that (real) of the excited metal nano-objects (Ni NPs) directly engaged in the RF-heated catalytic process. Besides the evident advantages of IH technology

applied to the methanation process in terms of process rates (λ) already under nominally low reaction temperatures, the virtual absence of any thermal inertia and the subsequent fast modulation of the temperature at the catalytic bed demonstrates unique features of this heating technology in terms of process safety (cold-reactor walls) and reduction of energy wastes (neither pre- and postcatalyst heating of reagents and products nor that of the whole reactor volume and its peripheral walls).

KEYWORDS: induction heating, methanation reaction, Joule heating, temperature of inductively heated nano-objects, SiC-based catalysts



INTRODUCTION

The development of integrated chemical strategies for the energy conversion and storage is a key priority of our modern society to address a truly renewable energy-based transition.¹ In the power-to-gas (P2G) chain, the exceeding amount of electrical energy produced from renewable and CO₂-free energy suppliers (i.e., wind, hydraulic, and solar) is converted into H₂ via water electrolysis. If not immediately used, H₂ can be employed as a reagent in CO₂ hydrogenation (Sabatier or methanation process)^{2–5} to give synthetic natural gas (SNG; CH₄). SNG is an energy vector of more practical use/management/distribution within the existing infrastructures and gas grids. Storage and transport conditions for methane are also easier and cheaper compared to those required for hydrogen.

CO₂ methanation is a highly exothermic process ($\Delta H^0 = -165 \text{ kJ mol}^{-1}$); nevertheless, it requires the use of catalysts along with large external heat input to overcome the severe kinetic limitations linked to CO₂ chemical inertness.⁶ External heating implies larger energy cost burdening on the process. In addition, its combination with the reaction exothermicity and

the thermal inertia of classically Joule-heated (JH) reactors hampers an accurate temperature control at the catalytic bed where local temperature gradients (hot spots) can be formed. The latter are typical sources of serious drawbacks and technical limitations linked to the catalyst stability and its performance on long-term runs other than representing a primary energy waste for the process.

In recent years, new achievements in catalysis have mainly pointed out on the process intensification⁷ by guaranteeing a quantum leap in its efficiency in terms of time, energy costs, employment of noncritical raw materials, and environmental impact rather than squeezing few percentages on the yield and selectivity of consolidated protocols of the state of the art. The electromagnetic induction heating (IH) or radiofrequency (RF)

Received: October 23, 2021

Revised: December 9, 2021

(RF) heating of electrically conductive or magnetic susceptors has already been exploited for a wide range of targeted applications, spanning from biomedical area^{8,9} in the treatment of diseases (through magnetic hyperthermia)¹⁰ to that of processes for metallurgic manufacturing.¹¹ Only recently, this technology has been exploited in catalysis,¹² spotlighting on the unique potentiality of this “noncontact” technology for the heat management in highly exo- and endothermic processes.¹² The possibility to convey heat only where it is needed for the chemical process using magnetically or electrically conductive susceptors/catalysts has been used to overcome several heat transfer limitations occurring in classical (Joule) heating schemes. IH indeed limits energy wastes associated to undesired and detrimental heating paths^{12,13} and drastically reduces the thermal inertia (heating/cooling rate) at the catalytic bed.¹²

As far as the CO₂ methanation reaction is concerned, IH has successfully been exploited by means of magnetic nanoparticles (NPs) and/or core-shell systems joining high hyperthermic efficiency^{14–16} to excellent catalytic performance. Similarly, electrically conductive susceptors decorated with catalytically active NPs have been employed as robust catalytic systems to run CO₂ hydrogenation under severe and dynamic conditions.¹² We have recently described an RF-heated methanation scheme based on highly Ni-loaded/ γ -Al₂O₃ (up to 40 wt %) composites as electrically conductive and magnetic susceptor/catalysts for rational heat management at the catalytic bed and with a drastic reduction in the nominal temperature values needed to efficiently perform the process [CO₂ conversion (X_{CO_2}) up to 98% with methane selectivity (S_{CH_4}) > 99% already at operative temperatures of 210–230 °C].¹³ Pieces of evidence from this study have led us to conclude that the catalyst temperature measured at the catalytic bed using a remote-sensing thermometer (pyrometer; ϕ laser beam: \approx 500 μm , power < 1 mW) is an average value between that of the support (γ -Al₂O₃) and that of the RF-excited nickel particles decorating its surface (catalytic sites). These results, together with others related from the literature,^{17,18} support the idea of a temperature gap between the value measured by the laser spot (macroscopic) and that (real) of the heated nano-objects (Ni NPs). Anyhow, the precise determination of the entity of this gap and thus the temperature value at the nanoscale remains a challenging task to be addressed,^{14,19–21} particularly in continuous flow, fixed-bed reactors operated under relatively harsh experimental conditions. Current technologies applied to this challenging task are generally based on the development and use of thermosensitive molecules as molecular temperature probes¹⁹ as well as advanced spectroscopic techniques as diagnostic tools for the determination of the local temperature values.²¹

This paper describes the design and synthesis of a new family of graphite felt (GF)-sandwiched ^kNi/SiC composites with variable metal loading ($k = 10, 15, \text{ and } 20 \text{ wt } \%$) as catalysts/susceptors for the methanation process to be operated under two distinct heating technologies: Joule heating (JH) versus IH. The choice of nickel as a metal active site is based on its renewed catalytic activity and stability in the process. Moreover, its magnetic properties make it a useful susceptor to run the process under IH conditions. SiC is a semiconductor, nonoxide ceramic featured by good thermal conductivity but not suitable to convert electromagnetism energy into heat (not RF-heatable).²² To improve the

hyperthermic efficiency of the catalytic system, Ni/SiC was sandwiched between two electrically conductive and IH-responsive (eddy or Foucault currents) GF disks. The comparative analysis of these catalytic materials under different heating configurations (JH vs IH) and experimental conditions [reaction temperature and gas hourly space velocity (GHSV)] has provided a practical tool for mapping the temperature gap existing between the macroscopic value measured at the catalyst bed using the pyrometer and that (real) of the excited metal nano-objects (Ni NPs) directly engaged in the RF-heated catalytic process.

At the same time, the catalytic study under IH has pointed out the superior performance of catalysts operated with this direct and noncontact heating technology together with its key advantages in terms of process safety (cold-reactor walls) and reduction of energy wastes.

EXPERIMENTAL SECTION

Materials and Methods. Silicon carbide (SiC) was purchased from Sicat SARL (www.sicatcatalyst.com) as mesoporous pellets ($3 \times 1 \text{ mm}$, $h \times \phi$)^{23–25} with a specific surface area (SSA) measured by a N₂ physisorption (at 77 K) of $27 \pm 3 \text{ m}^2 \text{ g}^{-1}$. SiC pellets were thoroughly washed with distilled water and oven-dried for several hours at 140 °C to remove all powdery fractions prior to be employed as supports for the preparation of the Ni-based composites. Unless otherwise stated, all other reagents and solvents were used as received by the providers without any specific purification/treatment.

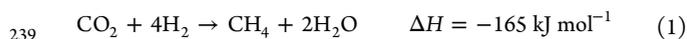
Synthesis of ^kNi/SiC Composites. In a typical procedure, SiC pellets (8 g) were impregnated with a proper amount (3.0, 4.8, and 6.8 mL) of a 5 M aqueous Ni(NO₃)₂·6H₂O solution to get ^kNi/SiC with a theoretical metal charge of $k = 10, 15, \text{ and } 20 \text{ wt } \%$, respectively. Impregnated samples were evaporated and oven-dried at 110 °C for 2 h before being calcined in air at 350 °C for 2 h as to prepare the corresponding metal oxides. The as-obtained ^kNiO/SiC precatalysts ($k = 10, 15, \text{ and } 20 \text{ wt } \%$) underwent reduction treatment under a pure H₂ flow (100 mL min⁻¹) at 350 °C for 2 h. This reduction step was accomplished as an in situ precatalyst treatment whatever may be the nature of the heating setup (JH or IH) employed for the CO₂ methanation trials. Scanning electron microscopy (SEM) was carried out on a ZEISS 2600F instrument with a resolution of 5 nm. A 10 kV electron beam was used for SEM imaging operated in the high vacuum mode, using BSE and SE detectors. For measurements, samples were deposited onto a double-face graphite tape holder as to avoid the charging effect during the analysis. Transmission electron microscopy (TEM) was carried out on a JEOL 2100F working at 200 kV accelerated voltage, equipped with a probe corrector for spherical aberrations, and a point-to-point resolution of 0.2 nm. Elemental mapping was finally accomplished by scanning transmission electron microscopy (STEM) on a JEOL 2100F electron microscope equipped with a Gatan Energy Filter and cold field-emission gun operated at 200 kV with 1.5 Å lattice resolution. For these measurements, samples were dispersed by ultrasound treatment (5 min) in an ethanol solution and a drop of each suspension was deposited on a copper grid covered with a holey carbon membrane for observation. Powder X-ray diffraction (PXRD) measurements were carried out on a D8 ADVANCE Bruker diffractometer with a Cu K α X-ray source ($\lambda = 1.5406 \text{ \AA}$). Rietveld refinements are performed using GSAS-II software.²⁶ The mean size of ordered (crystalline) domains (τ) is calculated from the Debye–Scherrer equation: $\tau = K\lambda/\beta \cos \theta$, where K is a shape factor, λ is the X-ray wavelength, β is the line broadening at half the maximum intensity (fwhm), and θ is the Bragg angle. The Brunauer–Emmett–Teller (BET) SSAs were calculated from N₂ physisorption isotherms recorded at 77 K on an ASAP 2020 Micromeritics instrument. Pore size distribution was determined by the Barrett–Joyner–Halenda (BJH) method applied to the desorption isotherm branches. Each sample was degassed/activated at 250 °C under vacuum for 8 h in order to desorb moisture and adsorbed species on its surface. Thermogravimetric analyses

189 (TGAs) were run under air (100 mL min^{-1}) on a TGA Q5000
 190 thermogravimetric analyzer (TG/DTA) using a heating rate of 10
 191 $^{\circ}\text{C/min}$. The average weight measured for each sample was
 192 maintained around 10 mg maximum. Inductively coupled plasma
 193 optical emission spectrophotometry (ICP-OES) measurements on
 194 mineralized $^k\text{NiO/SiC}$ precatalysts were accomplished on a Varian
 195 720 ES ICP-OES instrument. The IH setup (EasyHeat 8310, 4.2 kW ,
 196 Ambrell Ltd) is made of a six-turn spiral induction coil (length = 1.05
 197 m, pure coil resistance = $2.066 \times 10^{-3} \Omega$), cooled by means of an
 198 external chiller containing water/glycerol (10% , v/v) as the cooling
 199 mixture. For the temperature measurement in a typical RF-heated
 200 (IH) experiment, temperature at the catalyst bed was monitored/
 201 controlled/regulated in almost real-time using a PID system
 202 (proportional integral derivative controller, Eurotherm model 3504)
 203 connected to a laser pyrometer (Optris, ϕ laser beam: $\approx 500 \mu\text{m}$,
 204 power < 1 mW , located at $\approx 15 \text{ cm}$ from the catalyst and working in
 205 the $150\text{--}1000 \text{ }^{\circ}\text{C}$ range with an accuracy $\pm 1 \text{ }^{\circ}\text{C}$), shot up on the
 206 catalyst/susceptor. A standard calibration procedure²⁷ has been used
 207 to fix the emissivity factor for each $^k\text{Ni/SiC}$ ($k = 10, 15,$ and $20 \text{ wt } \%$)
 208 catalyst of the study. The heating/cooling rate allowed for the system
 209 was about $60\text{--}80 \text{ }^{\circ}\text{C min}^{-1}$ in the $150\text{--}300 \text{ }^{\circ}\text{C}$ temperature range.
 210 The inductor frequency was constantly maintained at $265 \pm 5 \text{ kHz}$,
 211 while the current flowing through the induction coils varied from 200
 212 to 450 A .

213 **IH Setup.** In a typical experiment, the quartz reactor containing the
 214 catalyst was housed inside the coils of the induction heater and
 215 temperature real-time control/regulation was ensured using a PID
 216 system (proportional integral derivative controller, Eurotherm model
 217 3504) connected to a laser pyrometer (remote-sensing thermometer)
 218 shot up on the catalyst bed (see Figure 3 for the sake of clarity).

219 **JH Setup (Electrical Oven).** In a typical experiment, the quartz
 220 reactor containing the catalyst was housed in an electrical oven
 221 (ERALY Co., $\phi_{\text{OD}} = 200 \text{ mm}$; $\phi_{\text{ID}} = 55 \text{ mm}$; depth: 300 mm ; $I_{\text{max}} =$
 222 8.6 A , and $T_{\text{max}} = 1100 \text{ }^{\circ}\text{C}$). The temperature of the system was
 223 monitored using two type-K thermocouples, one for regulating the
 224 oven temperature (T_{F}) and an additional one located in close contact
 225 with the catalytic bed (T_{C}) for measuring the temperature swings
 226 throughout the process. For these trials, we used thermocouples of
 227 ϕ_{ED} , 0.5 mm , very close to the dimension of the laser pyrometer spot
 228 in IH. Before each catalytic run, the catalyst was allowed to reach and
 229 stabilize ($30\text{--}45 \text{ min}$) at the target temperature under a pure stream
 230 of He (max temperature deviation recorded between T_{F} ($\text{F} = \text{furnace}$)
 231 and T_{C} ($\text{C} = \text{catalyst}$) after stabilization = $\pm 3 \text{ }^{\circ}\text{C}$) (see Figure 3 for
 232 the sake of clarity).

233 **Catalytic Tests.** The CO_2 methanation reaction (eq 1) was
 234 conducted at atmospheric pressure in a fixed-bed quartz tubular
 235 reactor ($\phi_{\text{ID}} = 12 \text{ mm}$ and length = 400 mm) charged with 0.6 g of the
 236 $^k\text{Ni/SiC}$ catalyst ($k = 10, 15,$ and $20 \text{ wt } \%$; $V \approx 0.8 \text{ cm}^3$) and housed
 237 on the proper heating setup (EasyHeat 8310 IH setup or a classical
 238 external furnace).



240 In a typical catalytic run, a H_2/CO_2 gas mixture (4 v/v) at variable
 241 GHSVs obtained by a series of calibrated mass flow controllers
 242 (Brookhorst) was continuously fed through the catalytic bed
 243 maintained at the target temperature. Gases at the reactor outlet
 244 are passed through a trap filled with silicon carbide pellets where
 245 water is condensed before reaching the gas chromatograph for
 246 analysis. Reactants and products were analyzed online at the
 247 respective reactor outlets using an R3000 (SRA Instrument) micro-
 248 gas chromatograph (μGC) equipped with an MSSA column for H_2 ,
 249 CH_4 , and CO detection and a PPU column for CO_2 and C_2 detection
 250 with a thermal conductivity detector (TCD). All reactors exit lines
 251 were maintained at $110 \text{ }^{\circ}\text{C}$ by external heating tapes as to avoid water
 252 condensation in the feed.

253 CO_2 conversion (X_{CO_2}) and CH_4 selectivity (S_{CH_4}) were calculated
 254 according to the following equations (eqs 2 and 3)

$$255 \quad X_{\text{CO}_2} (\%) = \frac{F_{\text{CO}_2(\text{in})} - F_{\text{CO}_2(\text{out})}}{F_{\text{CO}_2(\text{in})}} \times 100 \quad (2)$$

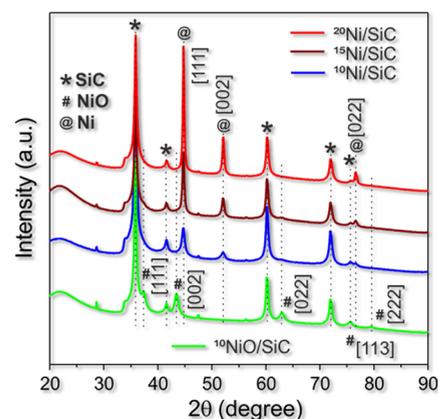
$$256 \quad S_{\text{CH}_4} (\%) = \frac{F_{\text{CH}_4(\text{out})}}{F_{\text{CH}_4(\text{out})} - F_{\text{CO}(\text{out})}} \times 100 \quad (3)$$

257 where $F_{i(\text{in/out})}$ (mL min^{-1}) is the flow rate of each component in the
 258 gas feed at the reactor inlet or outlet.

259 ■ RESULTS AND DISCUSSION

260 **Synthesis and Characterization of $^k\text{Ni/SiC}$ Catalysts ($k = 10, 15,$ and $20 \text{ wt } \%$).** $^k\text{Ni/SiC}$ composites ($k = 10, 15,$ or
 261 $20 \text{ wt } \%$) were straightforwardly prepared using a wet
 262 impregnation technique followed by conventional thermal
 263 calcination/reduction steps (see the Experimental Section for
 264 procedure details). The impregnated solids were oven-dried at
 265 $110 \text{ }^{\circ}\text{C}$ for 2 h and calcined in air at $350 \text{ }^{\circ}\text{C}$ for additional 2 h
 266 as to convert the nickel nitrate into its corresponding oxide.
 267 Catalysts were further reduced under a hydrogen flow (100 mL
 268 min^{-1}) at $350 \text{ }^{\circ}\text{C}$ for 2 h . All composites from this series were
 269 thoroughly characterized by PXRD, TEM/STEM, and N_2 -
 270 physisorption analyses, while their effective metal loading was
 271 determined (on NiO precatalysts) through ICP-OES measure-
 272 ments.

273 The catalyst composition and the average Ni NP size before
 274 and after the NiO reduction were systematically analyzed
 275 through PXRD. Figure 1 shows the PXRD patterns recorded
 276 ft



277 **Figure 1.** PXRD profiles of $^{10}\text{NiO/SiC}$ and $^k\text{Ni/SiC}$ ($k = 10, 15,$ and
 278 $20 \text{ wt } \%$) for comparison.

279 for the three $^k\text{Ni/SiC}$ ($k = 10, 15,$ and $20 \text{ wt } \%$) samples in
 280 comparison with the model system $^{10}\text{NiO/SiC}$, arbitrarily
 281 selected as a representative precatalytic system from this series.
 282 Hydrogenation (H_2 flow: 100 mL min^{-1} , at $350 \text{ }^{\circ}\text{C}$ for 2 h) of
 283 all calcinated precatalysts provides a complete NiO conversion
 284 into the corresponding Ni^0 particles. NiO diffraction peaks (at
 285 $2\theta = 37.3, 43.4, 63.0, 75.6,$ and 79.6° , respectively)²⁸ are
 286 almost quantitatively suppressed in all reduced samples, while
 287 new distinctive peaks ascribed to Ni^0 appear at $2\theta = 44.5, 51.8,$
 288 and 76.3° .²⁹ Expectedly, the peak intensity of the latter grows
 289 up appreciably when passing from 10 to $20 \text{ wt } \%$ of metal
 290 loading in the SiC normalized spectra. Notably, the chemical
 291 inertness of the SiC carrier is likely at the origin of the pure Ni^0
 292 phases obtained in all samples after the reduction step. The
 293 absence of strong chemical interactions between the metallic
 294 phase and the nonoxide ceramic support is witnessed by the
 295 absence of hardly reducible forms²² at the interface, resistant to

the relatively mild reduction conditions used. The Ni particle size was roughly estimated using the Scherrer equation³⁰ applied to the peak fwhm of diffraction peaks at $2\theta = 44.5$ and 51.8° . The mean values measured for the $^k\text{Ni}/\text{SiC}$ samples were fixed to 13 ± 1 , 21 ± 2 , and 26 ± 2 nm for $k = 10$, 15 , and 20 wt %, respectively.

The higher the metal loading, the higher is the mean nickel particle size and the generation of larger metal aggregates. While Ni/SiC composites at relatively low Ni contents (i.e., $^{10}\text{Ni}/\text{SiC}$) can boast a higher stability extent due to the presence of amorphous $\text{SiO}_2/\text{SiO}_x\text{C}_y$ layers at the carrier topmost surface that contribute to stabilize and disperse the metal active phase,^{22,31} higher metal loadings and larger metal aggregates on supports with moderate SSA are less leaching-resistant. As an example, SEM images of the $^{20}\text{Ni}/\text{SiC}$ catalyst (Figure S1) at different magnifications unveil the almost complete coating of the SiC carrier with nickel superstructures and structural vacancies; the latter are probably originated by the partial removal of poorly stabilized nickel aggregates. Therefore, the higher the metal content used in the catalysts' preparation, the higher the deviation between the theoretical and the effective metal loading in the composites. This trend was confirmed by the ICP-OES analysis on the final catalysts. While the $^{10}\text{Ni}/\text{SiC}$ sample showed an excellent match between the theoretical and the measured nickel loading (9.3 ± 0.3 wt %), $^{20}\text{Ni}/\text{SiC}$ displayed a higher deviation from the theoretical content (17.0 ± 0.8 wt %) (Table 1). At odds with

manuscript purposes, it can be simply claimed that the higher the metal charge, the lower is the SSA value of the composite.

TEM on $^k\text{Ni}/\text{SiC}$ (Figure 2A,B for $k = 10$ and Figure 2D,E for $k = 15$ wt %) showed a relatively homogeneous dispersion of metal NPs all over the SiC support. Moreover, a statistical analysis of NP size distribution carried out on each catalyst (Figure 2C,F) was in good agreement with PXRD outcomes. High-resolution (HR) TEM analysis (Figure S4) on $^{10}\text{Ni}/\text{SiC}$ has finally revealed the presence of crystalline phases featured by distinctive interplanar distances of 0.21 and 0.24 nm, characteristic of the (1 1 1) planes of Ni³³ and SiC³⁴ phases, respectively.

Methanation Reaction with $^k\text{Ni}/\text{SiC}$ as a Catalyst under Two Heating Configurations: JH Versus IH.

Looking for more efficient and energy-saving approaches to the methanation reaction, the $^k\text{Ni}/\text{SiC}$ ($k = 10, 15$, and 20 wt %) catalysts were investigated under two different reactor configurations: (i) a classical reactor scheme (Figure 3A) using an electrical furnace for the catalyst heating through convection, conduction, and/or radiation heat transfer (named hereafter as Joule-heating mode; JH) or (ii) an IH setup (Figure 3C) based on the electromagnetic properties of a susceptible medium (susceptor) exposed to a varying magnetic field (H) and its ability to convert the electromagnetic energy into heat at the catalytic bed or neighboring it (named hereafter induction-heating mode; IH).

For both reactors, temperature values were registered at the respective macroscopic heating sources. Therefore, for a JH system (Figure 3A), the temperature was monitored using two thermocouples housed in the furnace (temperature of the furnace, T_F) and in close contact with the quartz reactor (temperature of the catalyst, T_C), respectively. For the RF-heated setup (Figure 3C), the temperature was measured using a remote-sensing thermometer (pyrometer) with its laser beam directly shot over the GF susceptor (see the Experimental Section and Section 3.4 for details).

Whatever may be the heating configuration employed, $^k\text{Ni}/\text{SiC}$ powders were sandwiched in the quartz reactor between two GF disks (Figure 3B). The latter were innocent, porous, and thermal conductor supports for the catalytic material when the reaction was operated under the JH configuration (Figure 3A), whereas they exhibited the role of susceptors for the electromagnetic energy conversion into heat when the reaction was carried out under IH (Figure 3C; also see Section 3.4 for details). Blank tests carried out using the GF alone did not show any CO_2 methanation activity in the range of operational temperatures.

Effect of the Reaction Temperature and Heat Management Setup (JH vs IH) on the Methanation Performance.

In a first set of experiments, we studied the effect of the reaction temperature at the catalyst bed on its performance using both heating configurations (JH vs IH), while maintaining the amount of catalyst (600 mg) and the reagent GHSV ($10,000 \text{ mL g}^{-1} \text{ h}^{-1}$) constant. As Figure 4 shows, catalysis under JH (blue \bullet) presented classical sigmoidal trends for CO_2 (X_{CO_2}) conversion into SNG, whatever may be the catalytic system at work ($^k\text{Ni}/\text{SiC}$, $k = 10, 15$, and 20 wt %). Although $^{10}\text{Ni}/\text{SiC}$ reached the higher CO_2 conversion (X_{CO_2}) at 350°C (and kept it almost unchanged in the $350\text{--}375^\circ\text{C}$ range), $^{15}\text{Ni}/\text{SiC}$ and $^{20}\text{Ni}/\text{SiC}$ showed their higher performance at 375°C . As expected, the higher the nickel loading, the higher is the X_{CO_2} , although the

Table 1. ICP-OES Analysis, SSA, Pore Volume, and Pore Size Distribution Measured on Each $^k\text{Ni}/\text{SiC}$ ($k = 10, 15$, and 20 wt %) Composite in Comparison with the Bare Ceramic Support

entry	sample	Ni wt % (ICP-OES)	SSA ^a ($\text{m}^2 \text{g}^{-1}$)	total pore volume ^b ($\text{cm}^3 \text{g}^{-1}$)	average pore size ^c (nm)
1	SiC		27	0.16	23.8
2	$^{10}\text{Ni}/\text{SiC}$	9.3 ± 0.3	29	0.14	17.6
3	$^{15}\text{Ni}/\text{SiC}$	14.0 ± 0.5	26	0.13	21.6
4	$^{20}\text{Ni}/\text{SiC}$	17.0 ± 0.8	24	0.13	22.6

^aBET SSA measured at $T = 77 \text{ K}$. ^bTotal pore volume determined using the adsorption branch of the N_2 isotherm at $P/P_0 = 0.98$. ^cDetermined by BJH desorption average pore width ($4V/A$).

XRD data, XPS surface analyses of all Ni/SiC composites unveiled the presence of NiO_x forms (Figure S2A,B)³² resulting from a rapid passivation of metal deposits during the sample handling in air and their manipulation for analysis (formation of thin metal-oxide layers). For this reason, each NiO/SiC pre-catalyst underwent H_2 flow reduction at 350°C in situ (see the Experimental Section) just prior of its exposure to the reagents' mixture for catalysis. The SSA, the total pore volume, and the mean pore size measured for all Ni composites (Table 1, entries 2–4 and Figure S3B–D) were very similar and close to the morphological parameters recorded for the bare SiC support (Table 1, entry 1 and Figure S3A). All samples present classical type-II isothermal profiles and moderate SSA values. The meso–macroporous nature of the ceramic carrier was moderately affected by the deposition of Ni NPs and by the final metal loading in the composite. Although any conclusion based on these moderate morphological deviations remains speculative and poorly significant to the

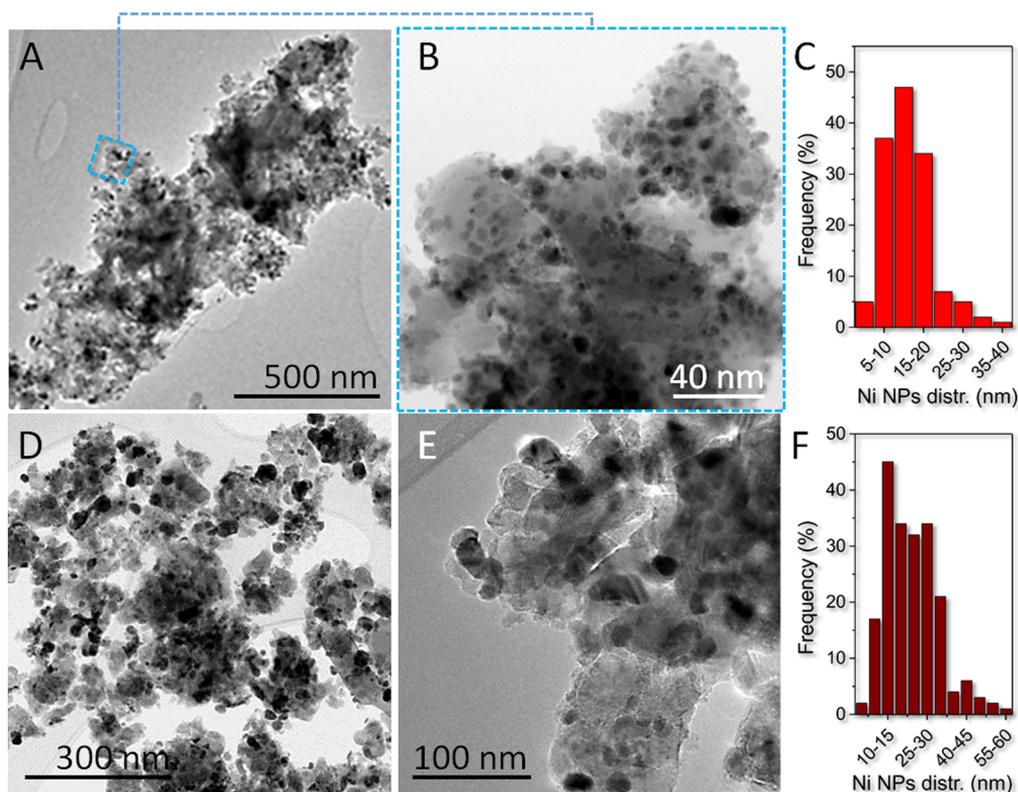


Figure 2. TEM images recorded on ¹⁰Ni/SiC (A,B) and ¹⁵Ni/SiC (D,E) at different magnifications along with the statistical distribution of NP sizes determined over 100 metal particles for each sample. (C,F) Ni NP size distribution on ¹⁰Ni/SiC and ¹⁵Ni/SiC, respectively.

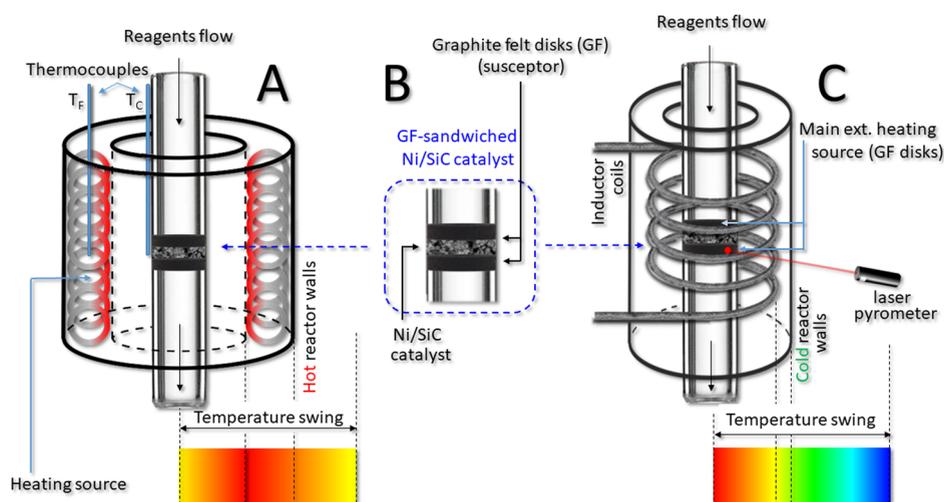


Figure 3. Representation of the adopted reactor configurations to carry out the methanation process; (A) electrical furnace (hot-wall reactor) operating with a classical JH scheme based on heat convection, conduction, and radiation; (B) details of the ^kNi/SiC catalyst sandwiched between two GF disks (susceptors) and housed in the quartz tube reactor; and (C) inductor coil for the RF heating of a susceptible medium (GF, susceptor) exposed to an external varying magnetic field (*H*). Thermal spectra reported below each reactor configuration account for the classical temperature diffusion (to and from the catalyst) depending on the operating heating technology (JH or contact and IH or contactless).

401 specific catalyst rate (λ) expressed as mol_{CH₄} produced per g_{Ni}
402 per *h* was superior with ¹⁰Ni/SiC (see Table S1).

403 Under these operative temperatures (<400 °C) and
404 irrespective of the employed heating setup, the SNG process
405 selectivity laid constantly close to 100% with no traces of CO
406 or other byproducts detected at the reactors' outlet. The
407 remarkably high S_{CH₄} was partially due to the thermal
408 conductivity of the SiC carrier²² that was thought to mitigate

the generation of local temperature gradients (hot spots) by
409 diffusing extra heat to the whole catalyst volume³⁵ and
410 ultimately favoring its removal by the action of the gaseous
411 reagent stream (solid–gas heat exchange).
412

Such a heat exchange was even more efficient in a RF-heated
413 catalyst because of the absence of reagents flow preheating
414 until they came in contact with the (hot) catalyst surface.
415

When CO₂ methanation was carried out under IH (red
416 ●), we observed an appreciably higher catalyst performance
417

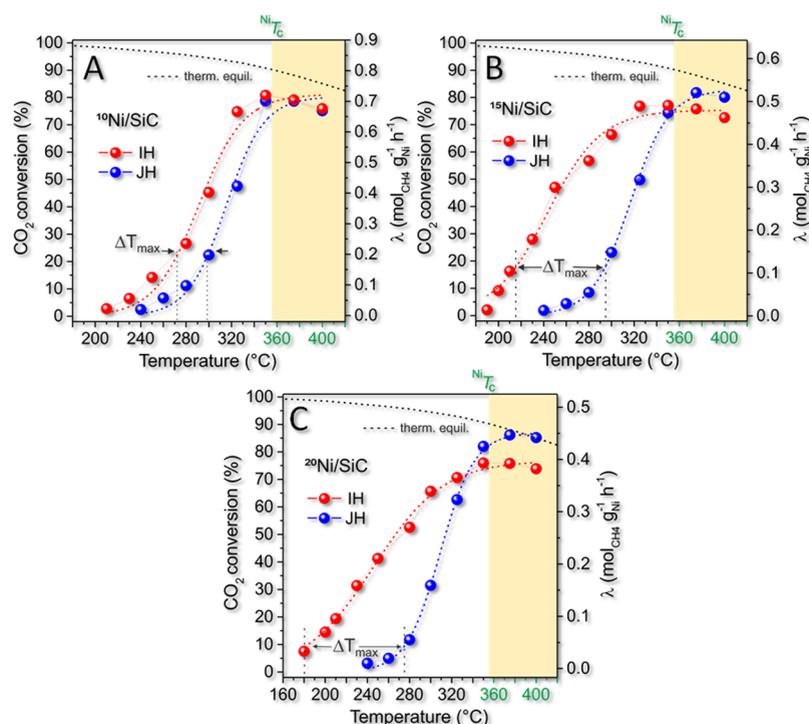


Figure 4. CO₂ methanation with ^kNi/SiC [*k* = 10 (A), 15 (B), and 20 wt % (C)] as a function of the reaction temperature. All catalysts were tested without any thermic diluent. Reaction conditions: catalyst weight = 600 mg, GHSV (STP) = 10,000 mL g⁻¹ h⁻¹, [CO₂] = 20 vol %, [H₂] = 80 vol %, H₂-to-CO₂ ratio = 4, total flow rate = 100 mL min⁻¹, atmospheric pressure. Red (●) and blue (●) curves refer to the X_{CO₂} vs temperature as experimentally determined within an IH and JH setup, respectively. CH₄ selectivity (S_{CH₄}, not shown in figures) was constantly equal to 100% in the whole temperature range. Thermodynamic equilibrium conversion (dashed black line “----”) has been included for the sake of comparison. All experimental data have been fitted with sigmoidal logistic functions of type I.

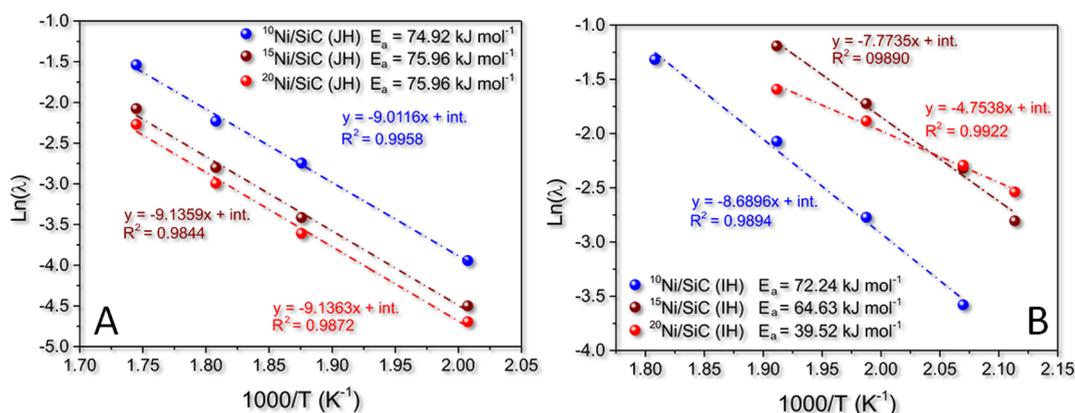


Figure 5. Arrhenius plots of ^kNi/SiC (*k* = 10, 15, and 20 wt %) in CO₂ methanation under the classical JH (A) or IH (B) setup. λ is expressed as mol_{CH₄} g_{Ni}⁻¹ h⁻¹ and measured in the temperature range where X_{CO₂} reaches 30% conversion maximum.

418 already for temperatures below 350 °C, whatever may be the
 419 metal loading of the catalyst at work. Remarkably, X_{CO₂}
 420 measured at 280 and 300 °C with ¹⁵Ni/SiC was up to 48
 421 and 43% higher than that measured under the same
 422 experimental conditions but for catalysts operated under the
 423 JH mode (Figure 4B). As a result, higher productivity values
 424 (λ) were recorded for the RF-heated ¹⁵Ni/SiC already at
 425 nominal low temperature (280 °C) values (Table S1). This
 426 result is of great relevance particularly in light of an industrial
 427 exploitation of these catalysts in combination with IH
 428 technology. The higher catalyst specific rate (λ) measured at
 429 low reaction temperatures with the RF-heated ¹⁵Ni/SiC fulfils

at least three key prerequisites of a sustainable methanation 430
 scheme: (i) catalysts with a relatively low loading of a highly 431
 dispersed and noncritical metal active phase; (ii) relatively 432
 mild operative temperatures to get high X_{CO₂} values chemo- 433
 selectively into SNG; and (iii) a safer and really energy-saving 434
 reactor configuration for the heat management at the catalytic 435
 bed. 436

It should be stressed that Ni composites at higher metal 437
 loading (i.e., ¹⁵Ni/SiC and ²⁰Ni/SiC) deviate appreciably from 438
 the classical sigmoidal profile when catalysis was operated 439
 under IH. Such a behavior was ascribed to a more complex 440
 heat management at the catalytic bed in the case of RF-heated 441

Table 2. Nickel Particle Size in the Three ^kNi/SiC (*k* = 10, 15, and 20 wt %) and Activation Energy Values (*E_a*) Calculated for the CO₂ Methanation Reaction Carried Out under JH or IH from the Respective Arrhenius Plots

entry	sample	Ni NPs ϕ (nm) ^a	<i>E_a</i> (JH) ^b (kJ mol ⁻¹)	<i>E_a</i> (IH) ^b (kJ mol ⁻¹)	ΔE_a (JH – IH) (kJ mol ⁻¹)	ΔT_{\max} (°C) ^c	<i>M_s</i> (emu/g) ^d
1	¹⁰ Ni/SiC	13 ± 1	75.0	72.2	2.8	26 ± 3	47.5 ± 0.7
2	¹⁵ Ni/SiC	21 ± 2	76.0	64.6	11.4	81 ± 4	51.2 ± 0.6
3	²⁰ Ni/SiC	26 ± 2	76.0	39.5	36.5	95 ± 4	52.4 ± 0.4

^aDetermined by XRD from the Scherrer equation and the peak fwhm of the diffraction peaks at $2\theta = 44.5$ and 51.8° . ^bCalculated from the curves' slopes of Arrhenius plots in the temperature range where X_{CO_2} reaches 30% conversion maximum. ^cDetermined as the maximum difference on the *x*-axis (ΔT , °C) of curves in Figure 4A,C between two points at the same CO₂ conversion (X_{CO_2} on JH and IH curves) as the maximum ΔT value (ΔT_{\max}) between the GF temperature (bulk temperature) and that effectively reached at the excited metal catalyst particle sites. ^dSpecific saturation magnetization (*M_s*) determined for the different Ni particle sizes on the basis of eq 4 and assuming a mean NiO layer of 0.5 nm in accordance with the TEM analysis on the samples of this study.

442 catalysts. Indeed, contributions to the catalyst heating derive in
 443 part from the inductively heated GF disks (heat transfer by
 444 convection/conduction to the thermally conductive SiC
 445 support), in part from dissipation paths related to the
 446 electrically conductive and magnetic nature of the large-sized
 447 Ni NPs (i.e., Eddy currents or Foucault currents and/or heat
 448 supplied via hysteresis losses).¹² As a proof of evidence, lower
 449 X_{CO_2} and λ values measured under IH for temperatures higher
 450 than 350 °C (Figure 4B,C) can be reasonably attributed to the
 451 loss of one heat dissipation path (e.g., heat hysteresis) as a
 452 function of the temperature effect on the metal magnetic
 453 properties (vide infra Section 3.4 for details).^{36,37}

454 Arrhenius plots (Figure 5) constructed as the logarithm of
 455 the catalyst process rate [$\text{Ln}(\lambda)$] versus the reciprocal of the
 456 reaction temperature (K^{-1}) have contributed to better
 457 distinguish among the catalytic performance of ^kNi/SiC
 458 catalysts operated under the two heating setups (Figure 3).
 459 Expectedly, when CO₂ methanation was carried out under the
 460 JH mode, the three catalysts behave similarly from a kinetic
 461 viewpoint, showing almost equal activation energy (curves'
 462 slope in Figure 5A and *E_a* values in Table 2) for processes
 463 operated under identical conditions. Moreover, calculated *E_a*
 464 values were in excellent agreement with the related literature
 465 data for the methanation process.^{38–40} Reversely, IH showed
 466 important deviations in the curves' slope (Figure 5B), hence
 467 implying relevant alterations of the activation energy values
 468 associated to the process.

469 As Table 2 shows, the higher the catalyst metal loading, the
 470 lower is the activation energy (*E_a*) for the inductively heated
 471 methanation process and thus the higher is the ΔE_a (JH – IH)
 472 gap measured for the reaction operated under different heating
 473 configurations.

474 It is evident that differences in the activation energy values
 475 (ΔE_a) measured for the same process, operated with the same
 476 catalyst but under different heating schemes (JH vs IH), had to
 477 be ascribed to the existence of a temperature gap between the
 478 value measured (macroscopically) at the GF surface and those
 479 (real) of the RF-heated nano-objects (nickel active sites) at the
 480 SiC surface.

481 Several precedents from the literature have already
 482 demonstrated the existence of important temperature discrep-
 483 ancies (up to orders of magnitude)¹⁷ between values reached
 484 at the surface of RF-heated nano-objects (metal NPs) and
 485 those measured macroscopically using a remote-sensing
 486 thermometer on the bulk materials.^{18,41–43} The temperature
 487 measurement at the level of single-catalyst particles (especially
 488 for magnetically responsive elements) remains a challenging
 489 issue to be addressed, and it becomes even more tricky under

operando conditions in severe experimental environ- 490
 ments.^{14,19–21} Anyhow, from the analysis of curves in Figure 491
 4A–C, it can be inferred that the maximum difference on the 492
x-axis (ΔT , °C) between two points at the same CO₂ 493
 conversion (X_{CO_2} on JH and IH curves) corresponds to the 494
 maximum ΔT value (ΔT_{\max}) between the “macroscopic” 495
 temperature measured at the GF disks and that actually 496
 reached at the RF-excited nickel particles. Accordingly, 26 ± 3 , 497
 81 ± 4 , and 95 ± 4 °C are the ΔT_{\max} values between GF and 498
 Ni NPs in the RF-heated Ni/SiC catalysts containing 10, 15, 499
 and 20 wt % of metal NPs, respectively. 500

As expected, such a ΔT value varies as a function of the 501
 magnetic properties of Ni NPs, hence their mean particle size 502
 as well as the dependence of the nickel specific saturation 503
 magnetization (*M_s*) from the temperature (Section 3.4 for 504
 details). 505

On the Origin of ΔT Values in RF-Heated ^kNi/SiC 506
Catalysts Applied to the CO₂ Methanation Reaction. 507
 There are no doubts that the two heating configurations (JH 508
 and IH) hold distinct thermal and energetic features. Indeed, 509
 the RF heating of a GF-sandwiched catalyst always occurs in a 510
 “cold-wall reactor” modality,²⁰ hence avoiding any pre- and 511
 postheating of reagents and products, including that of the 512
 whole reactor volume and its peripheral walls. Such a 513
 configuration fosters (among the others) the reaction 514
 thermodynamics by favoring H₂O condensation just after the 515
 (hot) catalytic bed and reduces all thermal inertia phenomena 516
 typically encountered on furnace-based reactors while 517
 guarantying more sustainable and energy-saving catalytic 518
 schemes.¹² 519

Similar benefits linked to a more convenient heat manage- 520
 ment at the catalytic reactor have recently been commented by 521
 others for different gas-phase processes.^{44,45} 522

It is clear that classical heat transfer by conduction/radiation 523
 (JH) applies to both heating configurations (JH and IH) 524
 proposed in this work. Under IH, the GF-sandwiched catalyst 525
 realizes a sort of micro-JH reactor. The thermal dissipation 526
 caused by the electromagnetically induced eddy currents 527
 flowing through the GF fibers can be considered as the main 528
 source of external heating (Figure 3B) for the catalyst active 529
 sites via classical conduction/radiation heat exchange. As an 530
 electrical semiconductor, SiC is not suitable to directly convert 531
 electromagnetic energy into heat at the catalytic bed; however, 532
 its thermal conductivity conveys the heat produced by the GF 533
 disks to the catalyst-active sites. Assuming the methanation 534
 exothermicity as independent from the nature of the adopted 535
 heating setup, under IH, the electrically conductive and 536
 magnetic nickel deposits (catalyst active phase) undergo 537

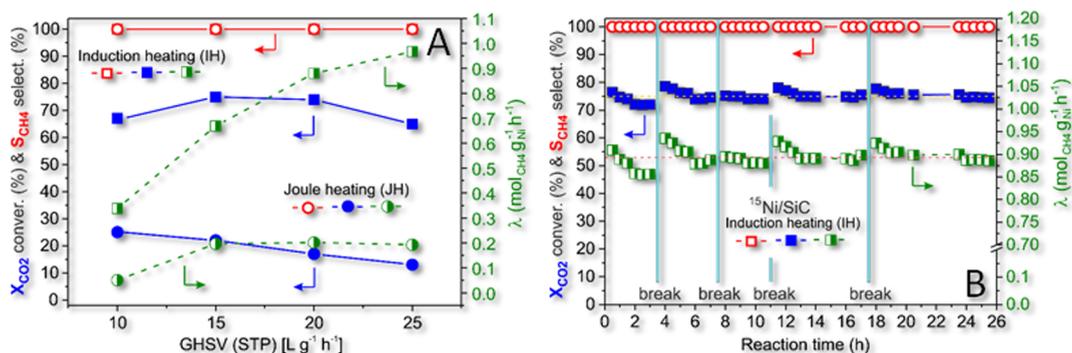


Figure 6. (A) X_{CO_2} and productivity rate (λ) dependence on the applied GHSV ($\text{L g}^{-1} \text{h}^{-1}$) for methanation processes operated on $^{15}\text{Ni}/\text{SiC}$ as a catalyst under the JH (round symbols) and IH (square symbols) mode. (B) Long-term methanation test at $20,000 \text{ mL g}^{-1} \text{h}^{-1}$ as GHSV under the discontinuous mode using the inductively heated $^{15}\text{Ni}/\text{SiC}$ catalyst. Each break corresponds to the reactor switching-off overnight. Other common reactional conditions for A and B: $[\text{CO}_2] = 20 \text{ vol } \%$; $[\text{H}_2] = 80 \text{ vol } \%$; H_2 -to- CO_2 ratio = 4; catalyst weight = 0.6 g; reaction temperature = $300 \text{ }^\circ\text{C}$, atmospheric pressure.

538 dedicated heating paths.⁴⁶ In particular, eddy currents (or
539 Foucault currents)^{47,48} flowing through the larger metal
540 aggregates and hysteresis loss^{49,50} phenomena can induce
541 local heating directly at the metallic phase. Hysteresis loss
542 depends from the specific saturation magnetization (M_s) of the
543 metal particles. It is a key property of ferromagnetic particles
544 and varies as a function of the metal NP size and their ultimate
545 temperature. Kuz'min demonstrated with a simple analytical
546 representation the shape of the temperature dependence⁵¹ for
547 bulk Ni NPs. He properly described the finite-temperature
548 properties of these ferromagnets in the $-273.15 \text{ }^\circ\text{C}$ Curie
549 temperature (T_C , $^\circ\text{C}$; $^{Ni}T_C = 355 \text{ }^\circ\text{C}$)⁵² range, with the latter
550 value corresponding to the temperature where M_s vanishes.³⁶
551 Duan and co-workers finally combined the morphological
552 properties (TEM and XRD) of various grain-sized Ni NPs
553 prepared by the autocatalytic reduction of a Ni^{II} salt with the
554 M_s size dependence. Their study provided a useful model for
555 the calculation of the experimental M_s value for similarly
556 prepared Ni NP-based catalysts in the form of spontaneously
557 surface-passivated (NiO-coated) systems like ours (see Section
558 3.1 for details). Based on their model (eq 4) and assuming a
559 mean size of our Ni NPs of 13, 21, and 26 nm with an average
560 thickness of the NiO thin layer for all catalysts of about 0.5 nm
561 (see also Figure S4B), we calculated M_s values comprised
562 between 47.5 and 52.4 emu/g (see Table 2), in excellent
563 accordance with the Ni NP size/ M_s dependence reported in
564 the literature.

$$M_s^{\text{exp}} = \frac{\sigma_s^{\text{bulk}} \times \frac{4}{3}\pi r^3 \times \rho_{\text{Ni}}}{\frac{4}{3}\pi r^3 \times \rho_{\text{Ni}} + \frac{4}{3}\pi(R^3 - r^3)\rho_{\text{NiO}}} \quad (4)$$

566 where $\rho_{\text{Ni}} = 8.8 \text{ g cm}^{-3}$, $\rho_{\text{NiO}} = 6.827 \text{ g cm}^{-3}$, $\sigma_s^{\text{bulk}} = 57.50$
567 emu/g, R = mean radius of Ni NPs from XRD analysis, and r =
568 (R – average thickness of a NiO thin layer).

569 The higher the M_s value, the higher is the hyperthermic
570 efficiency or specific absorption rate of the nickel-based sample
571 and thus the higher is its capacity to act as a heat susceptor⁵³
572 once immersed in an AC magnetic field.⁵⁴ The increasing
573 values of ΔT_{max} measured on Ni/SiC samples with variable
574 nickel-loading and nickel particle size (Figure 4A–C) are
575 perfectly in line with these conclusions. Interestingly, JH and
576 IH curves recorded in Figure 4A–C present similar converging
577 trends in close correspondence to the $^{Ni}T_C$ value ($355 \text{ }^\circ\text{C}$).
578 These trends led us to conclude that the extra heat (ΔT)

579 generated under IH at the catalytic nickel sites was essentially
580 due to hysteresis loss dissipation phenomena that were
581 definitively suppressed when the metal sites became para-
582 magnetic,^{55,56} that is, above $^{Ni}T_C$. Accordingly, it can be
583 concluded that eddy current contributions are almost
584 negligible, whatever may be the nickel loading in the three
585 catalysts in comparison. The moderate or null contribution
586 from eddy currents was finally confirmed by the increasing
587 X_{CO_2} conversion gap (or λ gap) measured with the two $^k\text{Ni}/$
588 SiC catalysts at higher metal loadings ($k = 15$ and $20 \text{ wt } \%$)
589 operated under JH and IH at temperatures $>355 \text{ }^\circ\text{C}$ (above
590 $^{Ni}T_C$). Under these conditions, the higher the catalyst particle
591 size, the higher is the X_{CO_2} conversion gap between the two
592 processes. Because eddy currents are directly proportional to
593 the square of the NP radius, their contribution should follow
594 an opposite trend to that recorded for catalysts $^{15}\text{Ni}/\text{SiC}$ and
595 $^{20}\text{Ni}/\text{SiC}$ operated in CO_2 methanation at temperatures $>^{Ni}T_C$.

596 According to the observed trends of X_{CO_2} versus temperature
597 recorded where the Ni NPs become paramagnetic (yellow
598 sections of Figure 4A–C), it can be concluded that catalyst
599 heating occurred through convection/conduction only. For the
600 two RF-heated catalysts at higher Ni loading ($^{15}\text{Ni}/\text{SiC}$ and
601 $^{20}\text{Ni}/\text{SiC}$), the reduced catalyst process rates for temperatures
602 $>^{Ni}T_C$ are then ascribed to a less-effective JH transfer in the
603 micro-JH reactor (GF-sandwiched catalyst) with respect to the
604 classical external furnace. In contrast with the classical furnace,
605 the formally cold walls of the micro-JH reactor facilitate a more
606 rapid heat dissipation from the catalytic bed. Therefore, it can
607 be inferred that this phenomenon in combination with the
608 suppressed magnetic properties of Ni particles further
609 contributed to the observed decrease in the catalysts'
610 performance.

611 **Effect of the Reactant Flow Rate (GHSV) on the**
612 **Methanation Performance of a JH or IH $^{15}\text{Ni}/\text{SiC}$**
613 **Catalyst.** The influence of the reactant space velocity
614 (GHSV) was deliberately investigated on $^{15}\text{Ni}/\text{SiC}$ as one of
615 the most representative samples from this catalyst series at a
616 temperature of $300 \text{ }^\circ\text{C}$ where the ΔX_{CO_2} and $\Delta \lambda$ values
617 were the highest (Figure 4B and Table S1, entries 15–16). As
618 Figure 6A shows, selectivity toward CH_4 laid constantly over
619 99% with no detectable traces of any other reaction byproduct,
620 whatever may be the adopted heating configuration and the gas

622 flow applied to the reactor in the 10–25 L g⁻¹ h⁻¹ GHSV
623 range.

624 As far as X_{CO₂} and λ values are concerned, the two heating
625 configurations translated into radically different catalyst
626 behaviors. Under the JH mode, X_{CO₂} decreased for increasing
627 flow rates and catalyst productivity (λ) remained substantially
628 unchanged throughout the last three reagent rates. When the
629 process was operated under IH, an initial X_{CO₂} increase was
630 observed and the catalyst productivity grew constantly (and
631 appreciably) for increasing reactant flows. It should be stressed
632 that Δλ in ¹⁵Ni/SiC operated under the two heating schemes
633 (JH and IH) and at increasing reactant flow rates (from 10,000
634 to 25,000 as GHSV) increased over 190% (Table S1, entries
635 15–16 vs 21–22). There were few doubts that different values
636 and trends in X_{CO₂} measured within the two heating
637 configurations at increasing GHSVs reflected a radically
638 different control of the temperature at the catalytic bed of
639 the two reactors. All X_{CO₂} decreasing trends measured at
640 increasing GHSVs can be claimed as the consequence of
641 several factors such as: (i) an oversaturation of the metal active
642 sites; (ii) a reduced contact time of reagents with the catalyst
643 active phase; and (iii) a reduced catalyst temperature due to a
644 more effective solid–gas heat exchange at increasing reactant
645 flow rates. All these phenomena may contribute to reducing
646 X_{CO₂} when GHSVs increase. However, i and ii items certainly
647 do not justify the growing trend of X_{CO₂} measured under IH
648 when the reaction was operated between 10,000 and 15,000
649 GHSVs. In contrast to classical JH reactors, temperature
650 swings at the catalytic bed caused by growing flow rates
651 (warming) and increased solid–gas heat exchanges (cooling)
652 are rapidly controlled and compensated (with almost no
653 thermal inertia) by a fast modulation of the current flowing
654 through the inductor coils (remote-sensing thermometer
655 connected to the inductor through a PID controller).

656 This excellent catalyst temperature control is also at the
657 origin of a prolonged stability and durability of inductively
658 heated catalysts on methanation run. Figure 6B refers to a
659 long-term methanation test operated with the RF-heated ¹⁵Ni/
660 SiC catalyst at 300 °C with 20,000 mL g⁻¹ h⁻¹ as GHSV and in
661 a discontinuous process (successive reactor shut-downs;
662 breaks) as to add a further stress factor to the long catalytic
663 trial (>25 h). As it can be seen, after an initial stabilization, the
664 catalyst constantly laid on an average X_{CO₂} = 75 ± 2% with a
665 quantitative methane selectivity and a productivity (λ) that
666 closely approached 0.9 mol_{CH₄} g_{Ni}⁻¹ h⁻¹.

667 The combination of the IH setup with the inherent thermal
668 conductivity of SiC supports reduces all classical drawbacks
669 associated to catalyst deactivation on run. TEM analysis of the
670 catalytic material before and after the long-term run has
671 demonstrated the superior stability of the catalytic system once
672 operated under IH. Indeed, neither relevant changes in the NP
673 size distribution (sintering) nor appreciable catalyst coking
674 phenomena after long-term runs were revealed (Figures S5 and
675 S6).

676 ■ CONCLUSIONS

677 In summary, we compared ^kNi/SiC composites at variable
678 metal loading as catalysts for the Sabatier process under two
679 different heating configurations (JH vs IH). The study has
680 unambiguously demonstrated the superior performance,

681 stability, and durability of catalysts operated under the less-
682 conventional IH setup. The superior performance of RF-
683 heated catalysts (already at relatively low temperatures)
684 basically stems from a different heat management at the
685 catalytic bed. The comparative analysis between the two
686 heating schemes along with the study of process kinetics has
687 offered a practical and simple tool to the estimation of the
688 temperature gap between that measured directly at the main
689 heat source and that (real) of the RF-heated nano-objects
690 (metal NPs). If we assume any catalyst heating/cooling
691 contributions (i.e., reaction exothermicity; solid–gas heat
692 exchanges at varying GHSVs; and heat dissipation by the
693 SiC support) as equal regardless of the nature of the heating
694 configuration at work (IH and JH), such a temperature
695 difference is unambiguously associated to the distinctive heat
696 dissipation properties (eddy currents and hysteresis loss) of the
697 electrically conductive and magnetic nickel particles immersed
698 in the AC magnetic field.

699 Besides the evident benefits of the IH technology applied to
700 the methanation process in terms of X_{CO₂} and process rates (λ)
701 already under nominally low reaction temperatures, the virtual
702 absence of thermal inertia phenomena and the subsequent fast
703 modulation of the temperature directly at the catalytic bed
704 hold unique advantages in terms of process safety (cold-reactor
705 walls) and reduction of energy wastes (neither pre- and
706 postcatalyst heating of reagents and products nor that of the
707 whole reactor volume and its peripheral walls). Finally, the
708 choice of silicon carbide as a support for the metal active phase
709 has guaranteed a better temperature control at the catalytic
710 bed. Indeed, SiC thermal conductivity allows the bidirectional
711 heat transfer between the GF disks (susceptors under IH) and
712 the Ni NPs, avoiding the formation of local hot spots that
713 reduce process selectivity and the catalyst lifetime.

714 ■ ASSOCIATED CONTENT

715 ■ Supporting Information

716 The Supporting Information is available free of charge at
717 <https://pubs.acs.org/doi/10.1021/acssuschemeng.1c07217>.

718 SEM, HRTEM, BET, and pore size distribution (BJH)
719 of ^kNi/SiC (*k* = 10, 15, and 20 wt %); XPS survey and
720 Ni 2p_{3/2} of ¹⁵Ni/SiC; and X_{CO₂} and catalyst specific rate
721 (λ) for CO₂ methanation with ^kNi/SiC (*k* = 10, 15, and
722 20 wt %) as catalyst(s) at variable reaction temperatures,
723 operated under the JH or IH mode (PDF)

724 ■ AUTHOR INFORMATION

725 Corresponding Authors

726 Lai Truong-Phuoc – Institute of Chemistry and Processes for
727 Energy, Environment and Health (ICPEES), ECPM, UMR
728 7515 of the CNRS and University of Strasbourg, 67087
729 Strasbourg Cedex 02, France; Email: [ltruongphuoc@](mailto:ltruongphuoc@unistra.fr)
730 unistra.fr

731 Giuliano Giambastiani – Institute of Chemistry and Processes
732 for Energy, Environment and Health (ICPEES), ECPM,
733 UMR 7515 of the CNRS and University of Strasbourg,
734 67087 Strasbourg Cedex 02, France; Institute of Chemistry of
735 Organometallic Compounds, ICCOM-CNR and Consorzio
736 INSTM, 50019 Florence, Italy; [orcid.org/0000-0002-](https://orcid.org/0000-0002-0315-3286)
737 [0315-3286](https://orcid.org/0000-0002-0315-3286); Email: giambastiani@unistra.fr,
738 giuliano.giambastiani@iccom.cnr.it

739 Cuong Pham-Huu – Institute of Chemistry and Processes for
740 Energy, Environment and Health (ICPEES), ECPM, UMR

741 7515 of the CNRS and University of Strasbourg, 67087
742 Strasbourg Cedex 02, France; Email: cuong.pham-huu@
743 unistra.fr

744 Authors

745 **Cuong Duong-Viet** – Institute of Chemistry and Processes for
746 Energy, Environment and Health (ICPEES), ECPM, UMR
747 7515 of the CNRS and University of Strasbourg, 67087
748 Strasbourg Cedex 02, France

749 **Giulia Tuci** – Institute of Chemistry of OrganoMetallic
750 Compounds, ICCOM-CNR and Consorzio INSTM, 50019
751 Florence, Italy; orcid.org/0000-0002-3411-989X

752 **Andrea Rossin** – Institute of Chemistry of OrganoMetallic
753 Compounds, ICCOM-CNR and Consorzio INSTM, 50019
754 Florence, Italy

755 **Jean-Mario Nhut** – Institute of Chemistry and Processes for
756 Energy, Environment and Health (ICPEES), ECPM, UMR
757 7515 of the CNRS and University of Strasbourg, 67087
758 Strasbourg Cedex 02, France

759 **Walid Baaziz** – Institute of Physic and Chemistry of Materials
760 of Strasbourg (IPCMS), UMR 7504 CNRS-University of
761 Strasbourg, 67037 Strasbourg Cedex 08, France

762 **Ovidiu Ersen** – Institute of Physic and Chemistry of Materials
763 of Strasbourg (IPCMS), UMR 7504 CNRS-University of
764 Strasbourg, 67037 Strasbourg Cedex 08, France;
765 orcid.org/0000-0002-1553-0915

766 **Mehdi Arab** – ORANO Tricastin, Direction de La Recherche
767 & Développement, 26701 Pierrelatte Cedex, France

768 **Alex Jourdan** – ORANO Tricastin, Direction de La Recherche
769 & Développement, 26701 Pierrelatte Cedex, France

770 Complete contact information is available at:
771 <https://pubs.acs.org/10.1021/acssuschemeng.1c07217>

772 Notes

773 The authors declare no competing financial interest.

774 ■ ACKNOWLEDGMENTS

775 The present work was supported by ORANO Co. through a
776 contract no. 40104671. G.G. and C.P.-H. would like to thank
777 the TRAINER project (Catalysts for Transition to Renewable
778 Energy Future) of the “Make our Planet Great Again” program
779 (Ref. ANR-17-MPGA-0017) for support. G.G. and G.T. would
780 also like to thank the Italian MIUR through the PRIN
781 2017Project Multi-e (20179337R7) “Multielectron transfer for
782 the conversion of small molecules: an enabling technology for
783 the chemical use of renewable energy” for financial support to
784 this work. The silicon carbide material was supplied by SICAT
785 SARL (www.sicatcatalyst.com), and Dr. Ch. Pham is gratefully
786 acknowledged for helpful discussion. SEM analysis was carried
787 out at the joint SEM platform of the ICPEES-IPCMS, and T.
788 Romero (ICPEES) is gratefully acknowledged for performing
789 the experiments.

790 ■ REFERENCES

791 (1) Götz, M.; Lefebvre, J.; Mörs, F.; McDaniel Koch, A.; Graf, F.;
792 Bajohr, S.; Reimert, T. Renewable Power-to-Gas: A technological and
793 economic review. *Renewable Energy* **2016**, *85*, 1371–1390.
794 (2) Centi, G.; Quadrelli, E. A.; Perathoner, S. Catalysis for CO₂
795 conversion: a key technology for rapid introduction of renewable
796 energy in the value chain of chemical industries. *Energy Environ. Sci.*
797 **2013**, *6*, 1711–1731.
798 (3) Hashimoto, K.; Kumagai, N.; Izumiya, K.; Takano, H.; Kato, Z.
799 The Production of Renewable Energy in the Form of Methane Using

Electrolytic Hydrogen Generation. *Energy, Sustainability and Society* **2014**, *4*, 17. 800
(4) Jentsch, M.; Trost, T.; Sterner, M. Optimal Use of Power-to-Gas 801
Energy Storage Systems in an 85% Renewable Energy Scenario. *802*
Energy Procedia **2014**, *46*, 254–261. 803
(5) Rönisch, S.; Schneider, J.; Matthischke, S.; Schlüter, M.; Götz, 804
M.; Lefebvre, J.; Prabhakaran, S. Review on methanation-from 805
fundamentals to current projects. *Fuel* **2016**, *166*, 276–296. 806
(6) Wang, W.; Wang, S.; Ma, X.; Gong, J. Recent advances in 807
catalytic hydrogenation of carbon dioxide. *Chem. Soc. Rev.* **2011**, *40*, 808
3703–3727. 809
(7) Stankiewicz, A.; Moulijn, J. A. Process Intensification. *Ind. Eng.* 810
Chem. Res. **2002**, *41*, 1920–1924. 811
(8) Timko, B. P.; Whitehead, K.; Gao, W.; Kohane, D. S.; 812
Farokhzad, O.; Anderson, D.; Langer, R. Advances in Drug Delivery. 813
Annu. Rev. Mater. Res. **2011**, *41*, 1–20. 814
(9) Norris, M. D.; Seidel, K.; Kirschning, A. Externally Induced Drug 815
Release Systems with Magnetic Nanoparticle Carriers: An Emerging 816
Field in Nanomedicine. *Adv. Ther.* **2019**, *2*, 1800092. 817
(10) Hedayatnasab, Z.; Abnisa, F.; Daud, W. M. A. W. Review on 818
magnetic nanoparticles for magnetic nanofluid hyperthermia 819
application. *Mater. Des.* **2017**, *123*, 174–196. 820
(11) Lozinskii, M. G. *Industrial Applications of Induction Heating*; 821
Pergamon: New York, NY, USA, 1969; p 690. 822
(12) Wang, W.; Duong-Viet, C.; Xu, Z.; Ba, H.; Tuci, G.; 823
Giambastiani, G.; Liu, Y.; Truong-Huu, T.; Nhut, J.-M.; Pham-Huu, 824
C. CO₂ Methanation Under Dynamic Operational Mode Using 825
Nickel Nanoparticles Decorated Carbon Felt (Ni/OCF) Combined 826
with Inductive Heating. *Catal. Today* **2020**, *357*, 214–220. 827
(13) Wang, W.; Duong-Viet, C.; Tuci, G.; Liu, Y.; Rossin, A.; 828
Luconi, L.; Nhut, J. M.; Nguyen-Dinh, L.; Giambastiani, G.; Pham- 829
Huu, C. Highly Nickel-Loaded γ -Alumina Composites for a 830
Radiofrequency-Heated, Low-Temperature CO₂ Methanation 831
Scheme. *ChemSusChem* **2020**, *13*, 5468–5479. 832
(14) Bordet, A.; Lacroix, L.-M.; Fazzini, P.-F.; Carrey, J.; Soulantica, 833
K.; Chaudret, B. Magnetically Induced Continuous CO₂ Hydro- 834
genation Using Composite Iron Carbide Nanoparticles of Exception- 835
ally High Heating Power. *Angew. Chem., Int. Ed.* **2016**, *55*, 15894– 836
15898. 837
(15) De Masi, D.; Asensio, J. M.; Fazzini, P. F.; Lacroix, L. M.; 838
Chaudret, B. Engineering Iron–Nickel Nanoparticles for Magnetically 839
Induced CO₂ Methanation in Continuous Flow. *Angew. Chem., Int.* 840
Ed. **2020**, *59*, 6187–6191. 841
(16) Rivas-Murias, B.; Asensio, J. M.; Mille, N.; Rodríguez-González, 842
B.; Fazzini, P. F.; Carrey, J.; Chaudret, B.; Salgueiriño, V. Magnetically 843
Induced CO₂ Methanation Using Exchange-Coupled Spinel Ferrites 844
in Cuboctahedron-Shaped Nanocrystals. *Angew. Chem., Int. Ed.* **2020**, 845
59, 15537–15542. 846
(17) Niether, C.; Faure, S.; Bordet, A.; Deseure, J.; Chatenet, M.; 847
Carrey, J.; Chaudret, B.; Rouet, A. Improved Water Electrolysis Using 848
Magnetic Heating of FeC–Ni Core-Shell Nanoparticles. *Nat. Energy* 849
2018, *3*, 476–483. 850
(18) Díaz-Puerto, Z. J.; Raya-Barón, Á.; van Leeuwen, P. W. N. M.; 851
Asensio, J. M.; Chaudret, B. Determination of the surface temperature 852
of magnetically heated nanoparticles using a catalytic approach. 853
Nanoscale **2021**, *13*, 12438–12442. 854
(19) Riedinger, A.; Guardia, P.; Curcio, A.; Garcia, M. A.; Cingolani, 855
R.; Manna, L.; Pellegrino, T. Subnanometer local temperature 856
probing and remotely controlled drug release based on azo- 857
functionalized iron oxide nanoparticles. *Nano Lett.* **2013**, *13*, 2399– 858
2406. 859
(20) Meffre, A.; Mehdaoui, B.; Connord, V.; Carrey, J.; Fazzini, P. 860
F.; Lachaize, S.; Respaud, M.; Chaudret, B. Complex Nano-objects 861
Displaying Both Magnetic and Catalytic Properties: A Proof of 862
Concept for Magnetically Induced Heterogeneous Catalysis. *Nano* 863
Lett. **2015**, *15*, 3241–3248. 864
(21) Hartman, T.; Geitenbeek, R. G.; Whiting, G. T.; Weckhuysen, 865
B. M. Operando monitoring of temperature and active species at the 866
single catalyst particle level. *Nat. Catal.* **2019**, *2*, 986–996. 867

- 869 (22) Tuci, G.; Liu, Y.; Rossin, A.; Guo, X.; Pham, C.; Giambastiani, G.; Pham-Huu, C. Porous Silicon Carbide (SiC): a Chance for
870 Improving Catalysts or just Another Active Phase Carrier? *Chem. Rev.* **2021**, *121*, 10559–10665.
- 873 (23) Ersen, O.; Florea, I.; Hirlimann, C.; Pham-Huu, C. Exploring
874 nanomaterials with 3D electron microscopy. *Mater. Today* **2015**, *18*,
875 395–408.
- 876 (24) Florea, I.; Ersen, O.; Hirlimann, C.; Roiban, L.; Deneuve, A.;
877 Houllé, M.; Janowska, I.; Nguyen, P.; Pham, C.; Pham-Huu, C.
878 Analytical electron tomography mapping of the SiC pore oxidation at
879 the nanoscale. *Nanoscale* **2010**, *2*, 2668–2678.
- 880 (25) Nguyen, P.; Pham, C. Innovative porous SiC-based materials:
881 From nanoscopic understandings to tunable carriers serving catalytic
882 needs. *Appl. Catal., A* **2011**, *391*, 443–454.
- 883 (26) Toby, B. H.; Von Dreele, R. B. GSAS-II: the genesis of a
884 modern open-source all purpose crystallography software package. *J.*
885 *Appl. Crystallogr.* **2013**, *46*, 544–549.
- 886 (27) For a standardized procedure see on “Datasheet & Manuals” at
887 the following link: <https://www.optris.global/optris-cslaser-lt> (ac-
888 cessed October, 2021).
- 889 (28) Cairns, R. W.; Ott, E. X-Ray Studies of the System Nickel—
890 Oxygen—Water. I. Nickelous Oxide and Hydroxide. *J. Am. Chem. Soc.*
891 **1933**, *55*, 527–533.
- 892 (29) Jette, E. R.; Foote, F. Precision Determination of Lattice
893 Constants. *J. Chem. Phys.* **1935**, *3*, 605–616.
- 894 (30) Jenkins, R.; Snyder, R. L. *Introduction to X-ray Powder*
895 *Diffraction*; John Wiley & Sons Inc., 1996; pp 89–91.
- 896 (31) Liu, Y.; Edouard, D.; Nguyen, L. D.; Begin, D.; Nguyen, P.;
897 Pham, C.; Pham-Huu, C. High Performance Structured Platelet Milli-
898 Reactor Filled with Supported Cobalt Open Cell SiC Foam Catalyst
899 for the Fischer-Tropsch Synthesis. *Chem. Eng. J.* **2013**, *222*, 265–273.
- 900 (32) Nesbitt, H. W.; Legrand, D.; Bancroft, G. M. Interpretation of
901 Ni2p XPS spectra of Ni conductors and Ni insulators. *Phys. Chem.*
902 *Miner.* **2000**, *27*, 357–366.
- 903 (33) Liu, B.; Liu, L. R.; Liu, X. J.; Liu, M. J.; Xiao, Y. S. Variation of
904 crystal structure in nickel nanoparticles filled in carbon nanotubes.
905 *Mater. Sci. Technol.* **2012**, *28*, 1345–1348.
- 906 (34) Lin, Y.-R.; Ho, C.-Y.; Chuang, W.-T.; Ku, C.-S.; Kai, J.-J.
907 Swelling of ion-irradiated 3C-SiC characterized by synchrotronra-
908 diation based XRD and TEM. *J. Nucl. Mater.* **2014**, *455*, 292–296.
- 909 (35) Pujula, M.; Sánchez-Rodríguez, D.; Lopez-Olmedo, J. P.; Farjas,
910 J.; Roura, P. Measuring thermal conductivity of powders with
911 differential scanning calorimetry. *J. Therm. Anal. Calorim.* **2016**,
912 *125*, 571–577.
- 913 (36) Chen, D.-X.; Pascu, O.; Roig, A.; Sanchez, A. Size analysis and
914 magnetic structure of nickel nanoparticles. *J. Magn. Magn.* **2010**, *322*,
915 3834–3840.
- 916 (37) He, X.; Zhong, W.; Au, C.-T.; Du, Y. Size dependence of the
917 magnetic properties of Ni nanoparticles prepared by thermal
918 decomposition method. *Nanoscale Res. Lett.* **2013**, *8*, 446.
- 919 (38) Li, L.; Zheng, J.; Liu, Y.; Wang, W.; Huang, Q.; Chu, W.
920 Impacts of SiC Carrier and Nickel Precursor of NiLa/support
921 Catalysts for CO₂ Selective Hydrogenation to Synthetic Natural Gas
922 (SNG). *ChemistrySelect* **2017**, *2*, 3750–3757.
- 923 (39) Vrijburg, W. L.; Moiola, E.; Chen, W.; Zhang, M.; Terlingen, B.
924 J. P.; Zijlstra, B.; Filot, I. A. W.; Züttel, A.; Pidko, E. A.; Hensen, E. J.
925 M. Efficient base-metal NiMn/TiO₂ catalyst for CO₂ methanation.
926 *ACS Catal.* **2019**, *9*, 7823–7839.
- 927 (40) Xu, L.; Wang, F.; Chen, M.; Nie, D.; Lian, X.; Lu, Z.; Chen, H.;
928 Zhang, K.; Ge, P. CO₂ methanation over rare earth doped Ni based
929 mesoporous catalysts with intensified low-temperature activity. *Int. J.*
930 *Hydrogen Energy* **2017**, *42*, 15523–15539.
- 931 (41) Asensio, J. M.; Miguel, A. B.; Fazzini, P. F.; van Leeuwen, P. W.
932 N. M.; Chaudret, B. Hydrodeoxygenation Using Magnetic Induction:
933 High-Temperature Heterogeneous Catalysis in Solution. *Angew.*
934 *Chem., Int. Ed.* **2019**, *58*, 11306–11310.
- 935 (42) Niether, C.; Faure, S.; Bordet, A.; Deseure, J.; Chatenet, M.;
936 Carrey, J.; Chaudret, B.; Rouet, A. Improved water electrolysis using
magnetic heating of FeC-Ni core-shell nanoparticles. *Nat. Energy* **2018**, *3*, 476.
- (43) Périco, E. A.; Hemery, G.; Sandre, O.; Ortega, D.; Garaio, E.;
Plazaola, F.; Teran, F. J. Fundamentals and advances in magnetic
hyperthermia. *Appl. Phys. Rev.* **2015**, *2*, 041302.
- (44) Julian, I.; Ramirez, H.; Hueso, J. L.; Mallada, R.; Santamaria, J.
Non-oxidative methane conversion in microwave-assisted structured
reactors. *Chem. Eng. J.* **2019**, *377*, 119764.
- (45) Ramirez, A.; Hueso, J. L.; Mallada, R.; Santamaria, J. In situ
temperature measurements in microwave-heated gas-solid catalytic
systems. Detection of hot spots and solid-fluid temperature gradients
in the ethylene epoxidation reaction. *Chem. Eng. J.* **2017**, *316*, 50–60.
- (46) Pearce, J.; Giustini, A.; Stigliano, R.; Jack Hoopes, P. Magnetic
Heating of Nanoparticles: The Importance of Particle Clustering to
Achieve Therapeutic Temperatures. *J. Nanotechnol. Eng. Med.* **2013**, *4*,
0110071–01100714.
- (47) Moses, A. J. Eddy current losses in soft magnetic materials. *Wiley Encyclopedia of Electrical and Electronics Engineering*; Wiley, 2016; pp 1–22.
- (48) Appino, A.; de la Barrière, O.; Fiorillo, F.; Lobue, M.;
Mazaleyrat, F.; Ragusa, C. Classical eddy current losses in Soft
Magnetic Composites. *J. Appl. Phys.* **2013**, *113*, 17A322–17A3223.
- (49) Ruta, S.; Chantrell, R.; Hovorka, O. Unified model of
hyperthermia via hysteresis heating in systems of interacting magnetic
nanoparticles. *Sci. Rep.* **2015**, *5*, 9090.
- (50) Hergt, R.; Dutz, S.; Röder, M. Effects of size distribution on
hysteresis losses of magnetic nanoparticles for hyperthermia. *J. Phys.: Condens. Matter* **2008**, *20*, 385214.
- (51) Kuz'min, M. D. Shape of Temperature Dependence of
Spontaneous Magnetization of Ferromagnets: Quantitative Analysis. *Phys. Rev. Lett.* **2005**, *94*, 107204.
- (52) Crangle, J.; Goodman, G. M. The Magnetization of pure iron
and nickel. *Proc. R. Soc. London, Ser. A* **1971**, *321*, 477.
- (53) Carrey, J.; Mehdaoui, B.; Respaud, M. Simple Models for
Dynamic Hysteresis Loop Calculations of Magnetic Single-Domain
Nanoparticles: Application to Magnetic Hyperthermia Optimization. *J. Appl. Phys.* **2011**, *109*, 083921.
- (54) Houlding, T. K.; Rebrov, E. V. Application of Alternative
Energy Forms in Catalytic Reactor Engineering. *Green Process. Synth.* **2012**, *1*, 19–31.
- (55) Sechovský, V. *Encyclopedia of Materials: Science and Technology*; Buschow, K. H. J., Cahn, R. W., Flemings, M. C., Ileschner, B., Kramer, E. J., Mahajan, S., Veyssiére, P., Eds.; Elsevier: Amsterdam, 2001; p 5021.
- (56) Frederikse, H. P. R. *Handbook of Chemistry and Physics*; *Properties of Magnetic Materials*; CRC Press LLC: Boca Raton, FL, 2009.